

Reversible on-off switching of both spin crossover and single-molecule magnet behaviours via a crystal-to-crystal transformation

Dong Shao,¹ Le Shi,¹ Lei Yin,² Bao-Lin Wang,³ Zhen-Xing Wang,^{2,*} Yi-Quan Zhang,^{3,*} Xin-Yi Wang^{1,*}

¹State Key Laboratory of Coordination Chemistry, Collaborative Innovation Center of Advanced Microstructures, School of Chemistry and Chemical Engineering, Nanjing University, Nanjing 210023, China.

²Wuhan National High Magnetic Field Centre, Huazhong University of Science and Technology, Wuhan 430074, China.

³Jiangsu Key Laboratory for NSLSCS, School of Physical Science and Technology, Nanjing Normal University, Nanjing, 210023, China.

* wangxy66@nju.edu.cn; zhangyiquan@njnu.edu.cn; zxwang@hust.edu.cn

Table of content

Experimental Section	3
Table S1. Data Collection and Structure Refinement Parameters for complexes 1 and 1-re ..	5
Table S2. Data Collection and Structure Refinement Parameters for 2	6
Table S3. Selected bond lengths (Å) and bond angles (°) for complexes 1 , 1-re , and 2	7
Table S4. Continuous Shape Measures calculation for 1 and 2	8
Figure S1. Thermogravimetric analysis..	9
Figure S2. UV-Vis spectra ..	11
Figure S3. Powder X-ray diffraction.....	12
Figure S4. Refinement of Powder X-ray diffraction of 1	10
Figure S5. Differential scanning calorimetry..	13
Figure S6. High-frequency and high-field electron paramagnetic resonance spectroscopy....	14
Computational details	15
Table S5. Calculated spin-free energies (cm ⁻¹) of the lowest ten terms ($S = 3/2$) of the Co ^{II} ion of complexes 1 and 2	16
Table S6. Calculated weights of the five most important spin-orbit-free states for the lowest two spin-orbit states of the Co ^{II} ion of complexes 1 and 2	17
Table S7. Calculated energy levels (cm ⁻¹), g (g_x , g_y , g_z) tensors of the ground and first excited doublets of the Co ^{II} of complexes 1 and 2	18
Figure S7. Calculated orientations of the local magnetic axes of the ground doublet on Co ^{II} ion of complexes 1 and 2	19
Figure S8. AC susceptibility of 1	20
Figure S9. AC susceptibility of 2	21
Figure S10. Argands plots of 2	22
Figure S11. AC susceptibility of 2	23
Figure S12. Argands plots of 2	24
Table S8. Relaxation fitting parameters at 3 K under different fields from the least-square fitting of the Cole-Cole plots of complex 2 according to the generalized Debye model.	25
Table S9. Relaxation fitting parameters at different temperatures under 1000 Oe from the least-square fitting of the Cole-Cole plots of 2 according to the generalized Debye model. ..	26
Figure S13. DC and AC susceptibilities of the rehydrated sample and its dehydrated form..	27
Table S10. Significant supramolecular interactions in 1	28
Supplementary discussion of the magnetic relaxation processes in 2	29
Supplementary References	31

Experimental Section

Materials and Synthesis. All reagents were commercially available and used as received without further purification. The powder of the starting material 4'-(4-Bromophenyl)-2,2':6',2''-terpyridine (**L**) was synthesized by the reaction of 4-bromobenzaldehyde, 2-acetylpyridine, KOH, and ammonia in ethanol under reflux to give a white solid. The crude product had poor solubility in common organic solvents and was purified by Soxhlet extraction into chloroform.

[Co(L)₂][DPAS]₂ DMF 2H₂O (1). A solution of Co(ClO₄)₂ 6H₂O (0.5 mmol, 182 mg) in 20 mL of H₂O was mixed with a hot solution of the Brphterpy ligand (1 mmol, 380 mg) in 40 mL DMF. Then, a solution of NaDPAS (1.8 mmol, 500 mg, NaDPAS = Sodium 4-(phenyl amino) benzenesulfonate) in 20 mL DMF was added to the above mixed solution. After heating for 5 min, the mixed dark red solution was then placed in a 100 mL bottle without seal, and left in the dark. X-ray suitable dark-red block-shaped crystals of **1** were obtained after slow evaporation for two weeks. The product was collected by filtration, washed with DMF/water, and dried in the air. Yield: 150 mg (20.8 %). Elemental analysis (%) for C₆₉H₅₈Br₂CoN₉O₉S₂: C, 57.54; H, 4.06; N, 8.75. Found: C, 57.41, H, 4.20; N, 8.58. IR (KBr, cm⁻¹): 3458 (m), 3399(m), 3271(vs), 3071(vs), 2821(w), 2720(w), 1665(vs), 1589 (vs), 1544(vs), 1494(vs), 1472(w), 1428(m), 1390 (vs), 1320(vs), 1445(m), 1249(w), 1208(w), 1175(w), 1118(w), 1073(w), 1027(vs), 1003(vs), 906(w), 831(w), 792(vs), 750(vs), 736(m), 723(s), 703(s), 656(s), 641(w), 621(w), 606(m), 585(w), 562(m), 503, 410(w).

[Co(L)₂][DPAS]₂ DMF (2). For SC-XRD measurement, a single crystal of **1** was dried in diffractometer under a dry nitrogen flow by heating from RT to 450 K at a heating rate of 3 K min⁻¹ and further annealing at 450 K for 2 h. Upon dehydration, the crystals changed its color from dark-red (**1**) to orange (**2**). For magnetic measurement, the well ground crystals of **1** were heated at 400 K in the dynamic vacuum chamber of SQUID VSM for 2 hours. For other physical measurements, the sample of **2** was prepared freshly by using the dynamic vacuum drying oven at 450 K for 2 h. Elemental analysis (%) for C₆₉H₅₄Br₂CoN₉O₇S₂: C, 59.02; H, 3.87; N, 8.97. Found: C, 58.91, H, 4.08; N, 8.68. IR (KBr, cm⁻¹): 3266(s), 3056(vs), 1664(vs), 1600(vs), 1589(vs), 1542(m), 1518(m), 1494(s), 1472(vs), 1454(w), 1428(vs), 1390(s), 1319(m), 1249(m), 1208(vs), 1176(vs), 1159(vs), 1120(vs), 1087(w), 1073(w), 1028(vs), 1003(vs), 920(w), 831(s), 793(s), 750(m), 704(s), 692(m), 584(m), 562(m), 502(m), 407(w).

[Co(L)₂][DPAS]₂ DMF 2H₂O (1-re). The single crystals of **1** were exposed at room-temperature to air atmosphere for one day. Elemental analysis (%) for C₆₉H₅₈Br₂CoN₉O₉S₂: C, 57.54; H, 4.06; N, 8.75. Found: C, 57.25, H, 4.29; N, 8.89. IR (KBr, cm⁻¹): 3468(m), 3396(m), 3299(s), 3071 (w), 1664(vs), 1611(vs), 1600(vs), 1589(vs), 1542(w), 1494(s), 1472(vs), 1428(vs), 1445(s), 1390(w), 1319(w), 1249(w), 1208(w), 1176(w), 1159(vs), 1120(vs), 1087(w), 1073(w), 1029(vs), 1003(vs), 920(w), 831(s), 793(s), 704(s), 584(w), 502(w).

Physical measurements. Infrared (IR) spectra data were measured on KBr pellets using a Nexus 870 FT-IR spectrometer in the range of 4000-400 cm^{-1} . Single-crystal UV-Vis spectra were obtained on a Craic Technologies microspectrophotometer. Elemental analyses of C, H, and N were performed at an Elementar Vario MICRO analyzer. Powder X-ray diffraction data (PXRD) were recorded at various temperatures on a Bruker D8 Advance diffractometer with Cu $K\alpha$ X-ray source ($\lambda = 1.54056 \text{ \AA}$) operated at 40 kV and 40 mA. Thermogravimetric analysis (TGA) was measured in Al_2O_3 crucibles using a PerkinElmer Thermal Analysis in the temperature range of 20-700 $^\circ\text{C}$ under flowing nitrogen at a heating rate of 20 $^\circ\text{C}/\text{min}$. Magnetic measurements from 2 to 400 K with dc field up to 70 kOe were performed using a Quantum Design SQUID VSM magnetometer on the grounded powders from the single crystals of the compounds. Alternative current (ac) magnetic susceptibility data were collected in a zero dc field or non-zero dc field in the temperature range of 2-10 K, under an ac field of 2 Oe, oscillating at frequencies in the range of 1-1000 Hz. All magnetic data were corrected for the diamagnetism of the sample holder and of the diamagnetic contribution of the sample.

HF-EPR Measurements. HF-EPR measurements for **1**, **2** and **1-re** were performed on a locally developed spectrometer at the Wuhan National High Magnetic Field Center, China. This facility is a transmission-type instrument, in which the microwaves are propagated by oversized cylindrical light pipes. The tunable microwave frequencies were provided by the combination of Gunn oscillators (Millitech) and backward wave oscillators (Institute of General Physics, Moscow, Russian Federation). The magnetic field was generated by a pulsed field magnet, and the detection was performed with an InSb hot-electron bolometer (QMC Ltd., Cardiff, U.K.). In order to minimize the field-induced torque effect, samples of **1**, **2** and **1-re** were ground, mixed with KBr, and pressed into pellets.

X-ray Crystallography. Single crystal X-ray crystallographic data were collected on a Bruker APEX Duo diffractometer with a CCD area detector (Mo- $K\alpha$ radiation, $\lambda = 0.71073 \text{ \AA}$). The APEXII program was used to determine the unit cell parameters and for data collection. The data were integrated and corrected for Lorentz and polarization effects using SAINT.^{S1} Absorption corrections were applied with SADABS.^{S2} The structures were solved by direct methods and refined by full-matrix least-squares method on F^2 using the SHELXTL crystallographic software package.^{S3} All the non-hydrogen atoms were refined anisotropically. Hydrogen atoms of the organic ligands were refined as riding on the corresponding non-hydrogen atoms. We used the methods of DIF-Fourier maps and HADD instructions to add the hydrogen atoms of the water molecules. Additional details of the data collections and structural refinement parameters are provided in Tables S1 and S2. Selected bond lengths and angles of **1** and **2** are listed in Table S3. **CCDC 1816022-1816026, and 1840937** are the supplementary crystallographic data for this paper. They can be obtained freely from the Cambridge Crystallographic Data Center via www.ccdc.cam.ac.uk/data_request/cif.

Table S1. Data Collection and Structure Refinement Parameters for complexes **1** and **1-re**.

Complex	1			1-re
Formula	C ₆₉ H ₅₈ Br ₂ CoN ₉ O ₉ S ₂₂			
Mr. / gmol ⁻¹	1440.12			
<i>T</i> , K	100	150	300	300
CCDC	1816022	1840937	1816023	
crystal system	Triclinic	Triclinic	Triclinic	Triclinic
space group	<i>P</i> 1	<i>P</i> 1	<i>P</i> 1	<i>P</i> 1
<i>a</i> [Å]	8.804(1)	8.8606(7)	8.933(2)	8.924(1)
<i>b</i> [Å]	13.872(1)	13.9125(10)	14.009(4)	14.002(16)
<i>c</i> , [Å]	15.012(1)	14.9455(11)	15.069(7)	15.174(16)
<i>α</i> [deg]	113.273(4)	65.422(2)	113.024(7)	113.120(14)
<i>β</i> [deg]	91.702(4)	87.897(2)	91.175(7)	91.073(16)
<i>γ</i> [deg]	108.265(4)	71.560(2)	108.218(6)	107.818(15)
<i>V</i> [Å ³]	1574.4(5)	1579.8(2)	1626.4(6)	1639(3)
<i>Z</i>	1	1	1	1
ρ_{calcd} [g cm ⁻³]	1.520	1.669	1.471	1.460
<i>F</i> (000)	737	736	734	737
<i>R</i> _{int}	0.0474	0.0515	0.0405	0.1193
<i>T</i> _{man} , <i>T</i> _{min}	0.8243, 0.5194	0.8248/0.6172	0.8292, 0.5290	0.8303, 0.5313
<i>R</i> ₁ , <i>wR</i> ₂ [<i>I</i> ≥ 2σ(<i>I</i>)] ^[a]	0.0681, 0.1583	0.0455, 0.1107	0.0531, 0.1237	0.0852, 0.2035
<i>R</i> ₁ , <i>wR</i> ₂ (all data)	0.0909, 0.1703	0.0521, 0.1148	0.0778, 0.1367	0.1540, 0.2326
^[a] GOF	1.041	0.997	1.022	1.047
Max/min /e [Å ⁻³]	1.020, -1.111	0.593, -0.636	0.685, -0.657	0.972, -0.968
^a R ₁ = ∑ F _o - F _c /∑ F _o ^b wR ₂ = {∑[w(F _o ² - F _c ²) ²]/ ∑[w(F _o ²) ²]} ^{1/2}				

Table S2. Data Collection and Structure Refinement Parameters for **2**.

Complex	2		
Formula	C ₆₉ H ₅₅ Br ₂ CoN ₉ O ₇ S ₂		
Mr. / gmol ⁻¹	1405.09		
<i>T</i> , K	150	300	450
CCDC	1816026	1816025	1816024
crystal system	Triclinic	Triclinic	Triclinic
space group	<i>P</i> 1	<i>P</i> 1	<i>P</i> 1
<i>a</i> [Å]	8.6306(4)	8.6715(5)	8.7198(4)
<i>b</i> [Å]	13.5529(7)	13.6890(8)	13.8688(7)
<i>c</i> , [Å]	15.2106(8)	15.1994(8)	15.1500(8)
<i>α</i> [deg]	113.1600(1)	112.725(2)	112.0760(1)
<i>β</i> [deg]	91.2520(1)	90.764(2)	90.1430(1)
<i>γ</i> [deg]	106.8630(1)	106.662(2)	106.4560(1)
<i>V</i> [Å ³]	1546.66(1)	1578.49(1)	1615.98(1)
<i>Z</i>	1	1	1
<i>ρ</i> _{calcd} [g cm ⁻³]	1.509	1.667	1.444
<i>F</i> (000)	717	717	717
<i>R</i> _{int}	0.0207	0.0232	0.0279
<i>T</i> _{max} , <i>T</i> _{min}	0.8219, 0.5149	0.8251, 0.5209	0.8286, 0.5279
<i>R</i> ₁ , <i>wR</i> ₂ [<i>I</i> ≥ 2σ(<i>I</i>)] ^[a]	0.0250, 0.0643	0.0380, 0.0983	0.0497, 0.1418
<i>R</i> ₁ , <i>wR</i> ₂ (all data) ^[a]	0.0265, 0.0649	0.0459, 0.1036	0.0579, 0.1507
GOF	1.011	1.054	1.053
Max/min /e [Å ⁻³]	0.623, -0.585	0.628, -0.796	0.576, -0.498
^a <i>R</i> ₁ = ∑ <i>F</i> _o - <i>F</i> _c /∑ <i>F</i> _o ^b <i>wR</i> ₂ = {∑[<i>w</i> (<i>F</i> _o ² - <i>F</i> _c ²) ²]/ ∑[<i>w</i> (<i>F</i> _o ²) ²]} ^{1/2}			

Table S3. Selected bond lengths (Å) and bond angles (°) for complexes **1**, **1-re**, and **2**.

Complex	1			1-re		2		
	T / K	100	150	300	300	150	300	450
Co1-N1		2.058(8)	2.080(4)	2.135(5)	2.128(1)	2.141(3)	2.143(4)	2.136(6)
Co1-N2		1.972(8)	1.987(4)	2.039(5)	2.047(1)	2.045(3)	2.040(3)	2.047(5)
Co1-N3		2.051(9)	2.075(5)	2.140(5)	2.157(1)	2.137(3)	2.137(4)	2.164(7)
Co1-N4		2.165(8)	2.151(4)	2.160(5)	2.155(1)	2.151(3)	2.148(4)	2.145(6)
Co1-N5		2.020(8)	2.003(4)	2.051(5)	2.030(1)	2.041(3)	2.042(3)	2.032(6)
Co1-N6		2.173(8)	2.172(4)	2.178(5)	2.184(1)	2.187(3)	2.183(4)	2.180(6)
Co-N_{average}		2.074	2.078(4)	2.117	2.116	2.117	2.116	2.118
Co-N _{center}		1.996(8)	1.995(4)	2.045(5)	2.038(6)	2.043(3)	2.041(3)	2.040(0)
Co-N _{dist}		2.112(6)	2.119(9)	2.153(8)	2.156(1)	2.154(0)	2.153(1)	2.156(8)
N1-Co1-N2		78.7(3)	78.1(7)	76.3(2)	75.6(4)	75.77(1)	75.63(1)	75.7(2)
N1-Co1-N3		155.9(3)	154.2(7)	151.2(2)	151.4(4)	151.08(1)	150.85(1)	150.7(2)
N1-Co1-N4		90.6(3)	90.7(1)	90.8(2)	90.8(5)	90.07(1)	89.87(1)	89.3(2)
N1-Co1-N5		105.4(3)	106.3(4)	107.9(2)	108.1(5)	109.05(1)	108.75(1)	107.7(2)
N1-Co1-N6		94.1(3)	95.2(8)	95.5(2)	95.6(5)	97.43(1)	97.50(1)	98.1(2)
N2-Co1-N4		111.8(3)	112.0(8)	112.7(2)	112.8(5)	115.24(1)	114.46(1)	113.6(3)
N2-Co1-N5		170.9(3)	170.6(3)	170.3(2)	170.3(5)	168.58(1)	169.07(1)	170.7(2)
N2-Co1-N6		94.0(3)	94.3(8)	94.9(2)	95.7(5)	93.06(1)	93.77(1)	94.9(2)
N3-Co1-N4		91.7(3)	91.2(0)	91.6(2)	91.9(5)	94.22(1)	94.47(1)	94.4(2)
N3-Co1-N5		98.4(3)	99.0(8)	100.6(2)	100.2(5)	99.70(1)	100.26(1)	101.4(2)
N3-Co1-N6		98.6(8)	94.3(6)	95.5(2)	95.4(5)	92.22(1)	92.19(1)	92.4(3)
N4-Co1-N5		75.7(7)	76.7(7)	76.4(2)	76.5(5)	75.56(1)	75.95(1)	75.4(2)
N5-Co1-N6		76.5(3)	76.8(7)	76.2(2)	75.2(5)	76.20(1)	75.87(1)	76.1(2)
Br1 ···Br2		3.438(7)	3.446(1)	3.467(8)	3.472(8)	3.427(9)	3.467(8)	3.477(8)
dihedral angle (deg) ^a		87.849	87.644	87.485	87.481	85.222	84.996	85.161
CShMs ^b		3.594	3.632	4.365	4.363	4.693	4.653	4.667
Σ ^c		88.9	89.1	90.4	90.4	91.5	91.7	91.4
Θ ^d		289	292	305	305	312	316	313

^aValue of the dihedral angle between the least-squares planes defined by the coordinated pyridyl rings of the two Brphterpy ligands. ^bCShMs: continuous shape measures values. ^cΣ is the sum of the deviation from 90° of the 12 cis angles of the CoN₆ octahedron. ^dΘ is the sum of the 24 unique N-Co-N angles measured on the projection of two triangular faces of the octahedron along their common pseudo-3-fold axis.

Table S4. Continuous Shape Measures calculation for **1** and **2**.

Symmetry	Shape	Deviation value (CShMs)					
		Co	1			2	
	T, K	100	150	300	150	300	450
<i>D</i> _{6h}	Hexagon	33.176	33.285	33.883	32.498	32.609	32.835
<i>C</i> _{5v}	Pentagonal pyramid	19.669	19.485	18.765	17.981	18.045	18.257
<i>O</i> _h	Octahedron	3.594	3.632	4.365	4.693	4.653	4.667
<i>D</i> _{3h}	Trigonal prism	9.365	9.120	8.900	9.030	9.209	9.573
<i>C</i> _{5v}	Johnson pentagonal pyramid	23.393	23.123	22.729	21.810	21.884	22.222

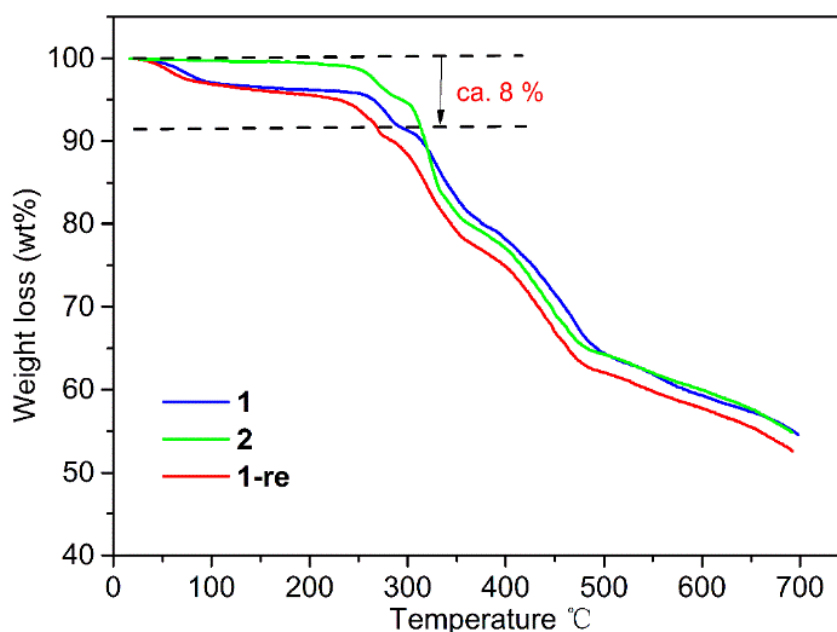


Figure S1. Thermogravimetric analysis. The solid blue, green, red lines represent the TGA data of compounds **1**, **2** and **1-re**, respectively. The TGA of **1** reveals that the desolvation process occurred within the 20-320 °C range in two steps. In the first step at 20-80 °C, the crystallization water molecules are released with a weight loss of ca. 3% to give the **2**. Experiencing a wide terrace between 80 to 250 °C, the remaining DMF molecules (ca. 5.1%) are liberated in the second step in the 250-290 °C range. This two-step processes of weight loss correspond to the removal of water molecules (calcu. 2.5 %) and DMF (calcu. 5.07 %) in **1**. The green line clearly shows a wide terrace between 20 to 250 °C, and then begins to loss weight. The red line has a very similar curve with **1**. These lines also supported the reversible dehydration/rehydration process between **1** and **2**.

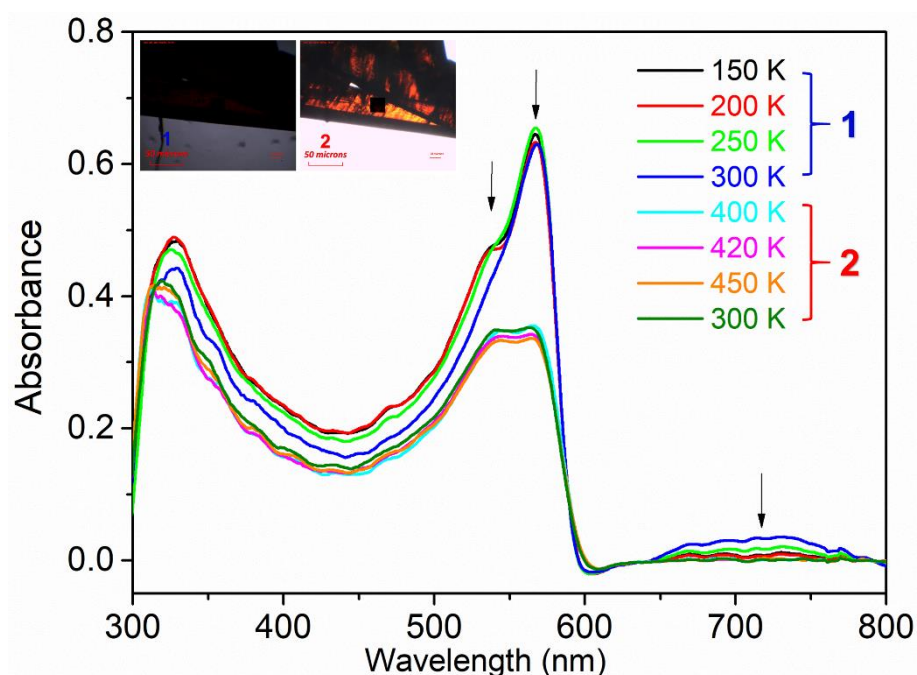


Figure S2. UV-Vis spectra. The variable-temperature single-crystal UV-Vis spectra of 1 and 2 were conducted to investigate the color change during the dehydration. The measurement was carried out from low temperature to high temperature and back to room temperature again (Figure S3). As can be seen, there are clear differences between the spectra of 1 and 2. Upon warming from 150 to 300 K, the maximum adsorption peak (567 nm) kept unchanged during the gradual spin transition, while the relatively small adsorption peak around 545 nm disappeared. A distinct change was observed as a result of single-crystal-to-single-crystal transformation. The intensity of the sharp adsorption peak at 567 nm decreases and the broad adsorption peak around 725 nm flattened. These results correspond to the color switching from dark-red to orange of the single crystal during dehydration.

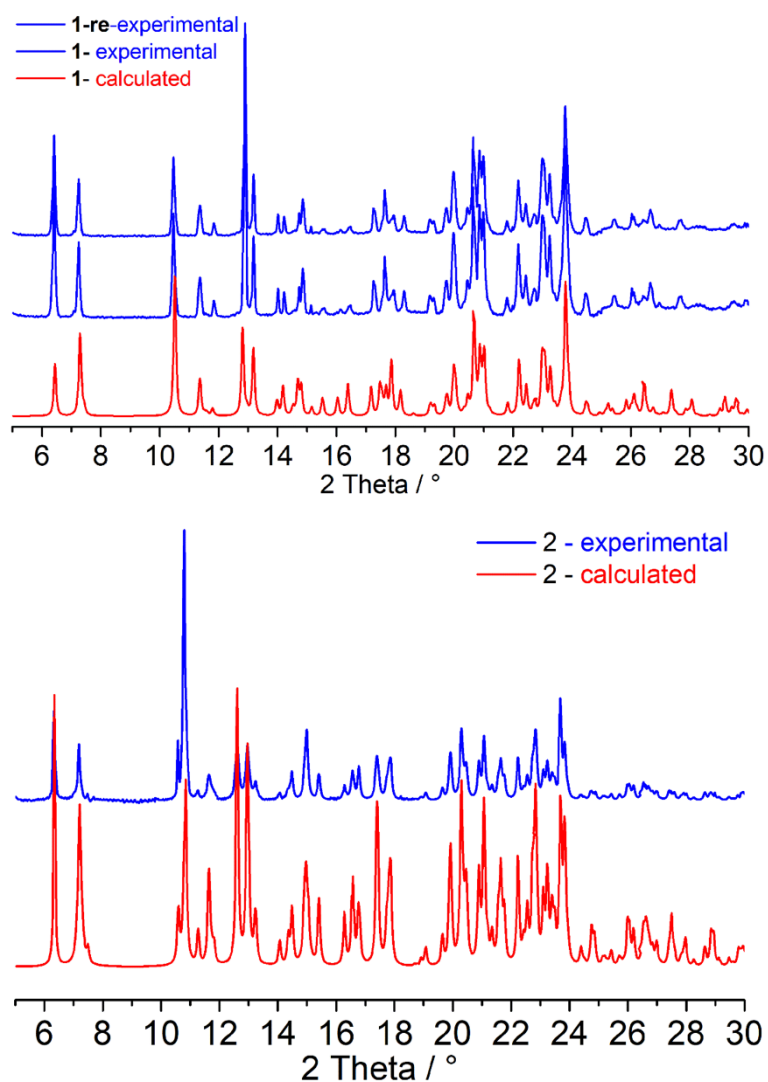


Figure S3. Powder X-ray diffraction. The solid blue and red lines represent the experimental and calculated powder XRD patterns for **1**, **1-re** and **2**, respectively. The dehydration process clearly caused distinct shifting and appearance of some peaks. However, these peaks return to their original state again after rehydration. Thus, the reversible dehydration/rehydration process is also supported by these PXRD data.

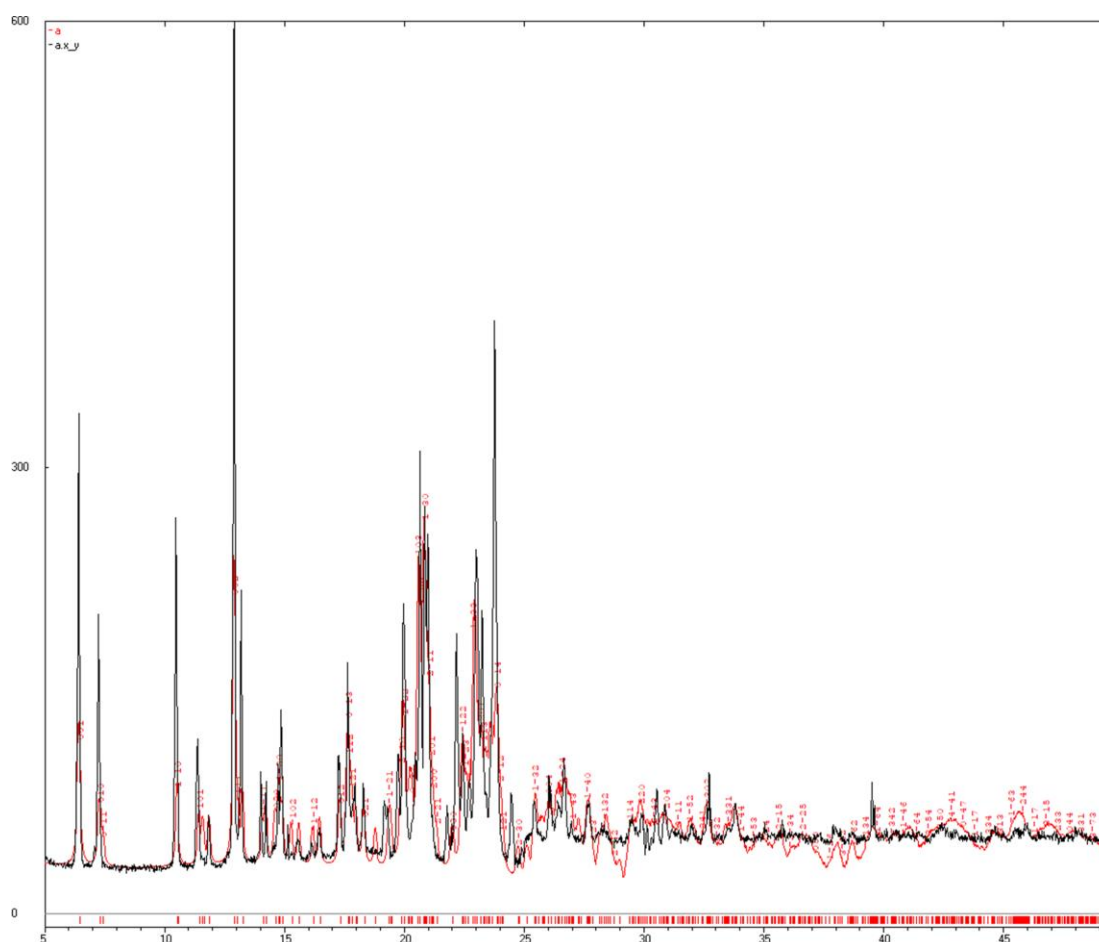


Figure S4. Refinement of Powder X-ray diffraction of 1. The solid black and red lines represent the experimental and refined powder XRD patterns for **1**, respectively. As can be seen in Table S1, the lattice parameters from crystal data ($a = 8.933(2) \text{ \AA}$, $b = 14.009(4) \text{ \AA}$, $c = 15.069(7) \text{ \AA}$, $\alpha = 113.024(7)^\circ$, $\beta = 91.175(7)^\circ$, $\gamma = 108.218(6)^\circ$) are close to the obtained refinement parameters ($a = 8.93 \text{ \AA}$, $b = 14.02 \text{ \AA}$, $c = 15.08(4) \text{ \AA}$, $\alpha = 113.03^\circ$, $\beta = 91.18^\circ$, $\gamma = 108.18^\circ$). This result provides a further proof of the correct choice of $P1$ space group for **1**.

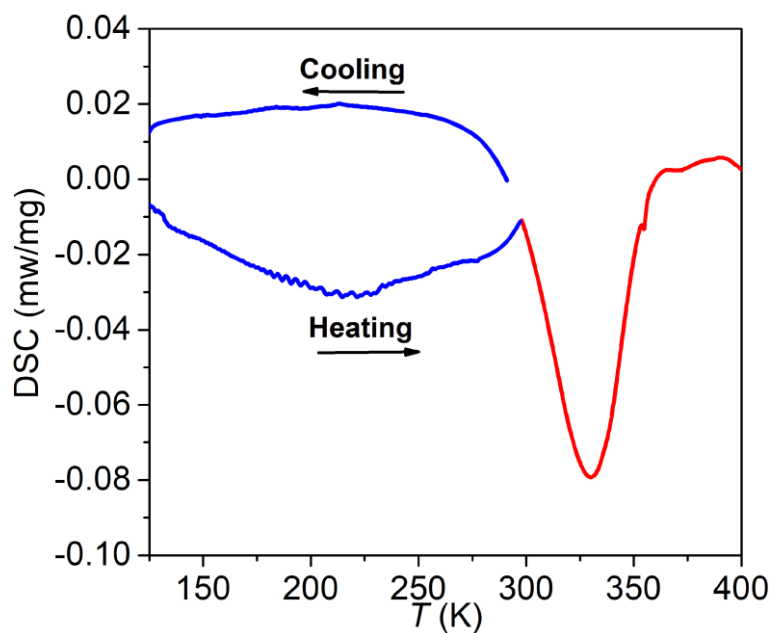


Figure S5. Differential scanning calorimetry. The red DSC curve corresponds to the loss of water molecules and to the single-crystal-to-single-crystal structural phase transition.

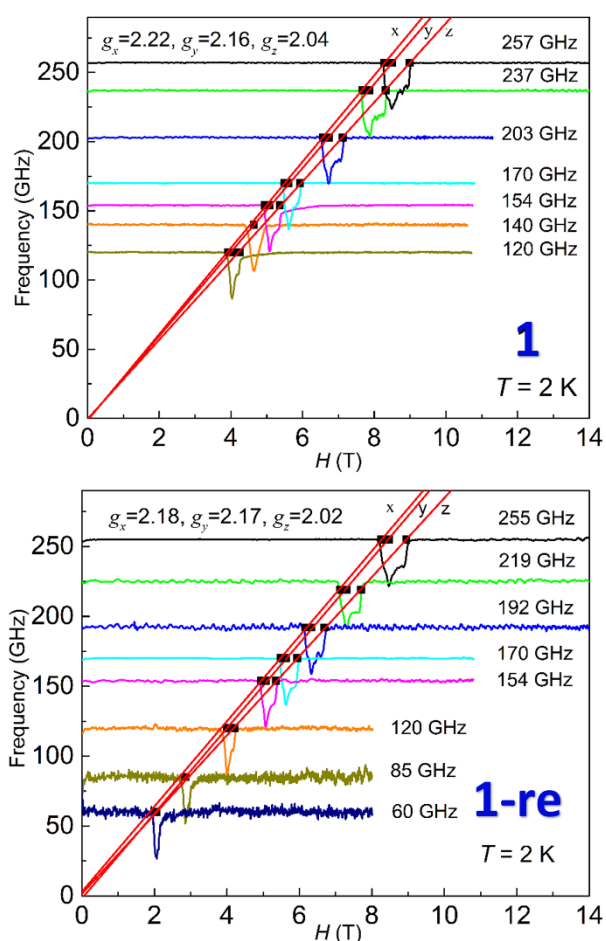


Figure S6. High-frequency and high-field electron paramagnetic resonance spectroscopy. Microwave frequency vs resonance field of EPR transitions for **1** and **1-re** at 2 K. The solid lines are the simulations with the Hamiltonian parameters: $S = 1/2$, $g_x = 2.22(2)$, $g_y = 2.16(2)$, $g_z = 2.04(2)$ for **1** and $S = 0.5$, $g_x = 2.18(2)$, $g_y = 2.17(2)$, $g_z = 2.02(2)$ for **1-re**. These almost same results clearly show typical $S = 1/2$ signals as expected for a LS state of **1** and **1-re** at 2 K, and also indirectly support the reversible dehydration/rehydration process.

Computational details

Complete active space second-order multiconfigurational perturbation theory (CASPT2) considering the effect of the dynamic electron correlation based on complete-active-space self-consistent field (CASSCF) method with MOLCAS 8.2 program package^{S4} was performed on individual Co^{II} fragment (see Figure. S13 for the calculated structures of complexes **1–2**) on the basis of X-ray determined geometry of complexes **1–2**. During the calculations, the basis sets for all atoms are atomic natural orbitals from the MOLCAS ANO-RCC library: ANO-RCC-VTZP for Co^{II} ion; VTZ for close N; VDZ for distant atoms. The calculations employed the second order Douglas-Kroll-Hess Hamiltonian, where scalar relativistic contractions were taken into account in the basis set. After that, the effect of the dynamical electronic correlation was applied using CASPT2. And then, the spin-orbit couplings were handled separately in the restricted active space state interaction (RASSI-SO) procedure. The active electrons in 10 active spaces considering the 3*d*-double shell effect (5+5) include all seven 3*d* electrons (CAS (7 in 5+5)), and the mixed spin-free states are 30 (all from 10 quadruplets and 20 from 40 doublets).

Table S5. Calculated spin-free energies (cm^{-1}) of the lowest ten terms ($S = 3/2$) of the Co^{II} ion of complexes **1** and **2**.

spin-free states	1			2	
	100K E/cm^{-1}	300K E/cm^{-1}	150K E/cm^{-1}	300K E/cm^{-1}	450K E/cm^{-1}
1	0.0	0.0	0.0	0.0	0.0
2	566.1	512.7	453.2	418.3	349.1
3	1367.1	1451.1	1513.3	1432.3	1356.0
4	9999.8	9287.3	9176.8	9111.9	9083.4
5	12178.6	9755.7	9697.8	9672.5	9344.1
6	13458.2	11443.5	11303.7	11418.0	11591.1
7	22248.8	20350.4	20008.9	20123.6	20075.0
8	22802.3	20507.7	20308.0	20413.5	20627.9
9	25059.0	22714.4	22359.2	22305.6	22327.3
10	25599.2	22991.6	23143.3	23150.7	23141.8

Table S6. Calculated weights of the five most important spin-orbit-free states for the lowest two spin-orbit states of the Co^{II} ion of complexes **1** and **2**.

Spin-orbit states		Energy (cm ⁻¹)	Spin-free states Spin Weights					
1	100K	1	0.0	1, 1.5 0.7644	2, 1.5 0.1954	3, 1.5 0.0383	22, 0.5 0.0004	4, 1.5 0.0003
		2	133.4	1, 1.5 0.9248	2, 1.5 0.0511	3, 1.5 0.0181	11, 0.5 0.0022	5, 1.5 0.0012
	300K	1	0.0	1 1.5 0.7374	2 1.5 0.2299	3 1.5 0.0305	5 1.5 0.0005	22, 0.5 0.0005
		2	157.2	1, 1.5 0.9166	2, 1.5 0.0592	3 1.5 0.0187	5 1.5 0.0018	4 1.5 0.0008
	150K	1	0.0	1 1.5 0.7167	2 1.5 0.2547	3 1.5 0.0264	5 1.5 0.0005	22 0.5 0.0004
		2	167.8	1 1.5 0.9073	2 1.5 0.0690	3 1.5 0.0183	5 1.5 0.0017	4 1.5 0.0008
2	300K	1	0.0	1 1.5 0.6998	2 1.5 0.2686	3 1.5 0.0293	5 1.5 0.0005	22 0.5 0.0005
		2	173.2	1 1.5 0.8978	2 1.5 0.0772	3 1.5 0.0196	5 1.5 0.0017	4 1.5 0.0009
	450K	1	0.0	1 1.5 0.6638	2 1.5 0.3032	3 1.5 0.0309	5 1.5 0.0005	22 0.5 0.0004
		2	186.6	1, 1.5 0.8758	2, 1.5 0.0982	3 1.5 0.0205	5 1.5 0.0016	4 1.5 0.0011

Table S7. Calculated energy levels (cm^{-1}), g (g_x, g_y, g_z) tensors of the ground and first excited doublets of the Co^{II} of complexes **1** and **2**.

		1				2					
		100K		300K		150K		300K		450K	
		E/cm^{-1}	g								
1		1.685		1.396		1.257		1.314		1.306	
	0.0	2.448		1.781		1.537		1.592		1.488	
		7.444		8.075		8.304		8.289		8.401	
2		2.130		2.631		2.775		2.683		2.610	
	133.4	2.188		2.781		3.012		3.034		3.242	
		5.249		4.887		4.664		4.615		4.363	

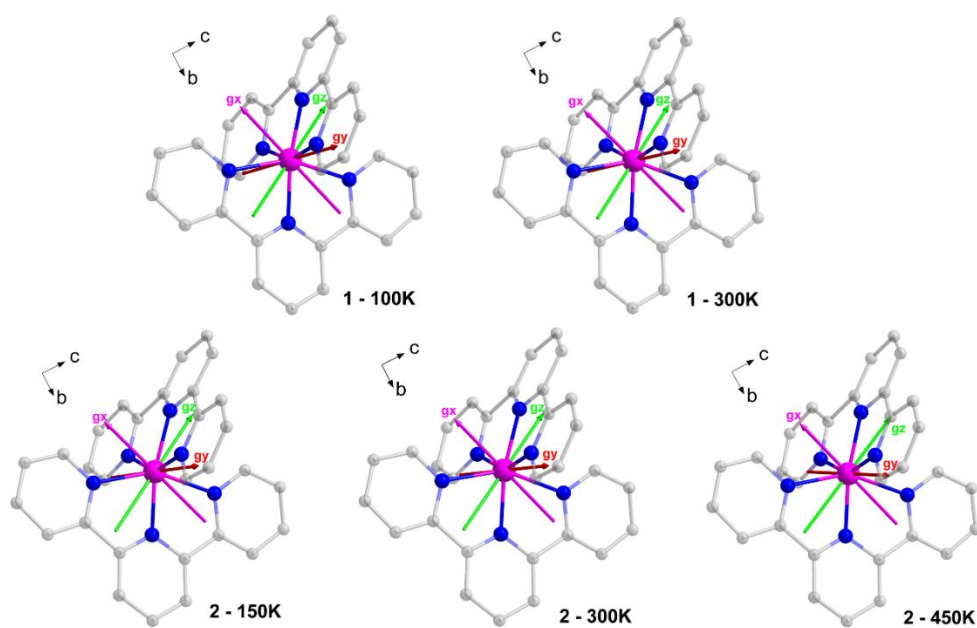


Figure S7. Calculated orientations of the local magnetic axes of the ground doublet on Co^{II} ion of complexes **1** and **2**.

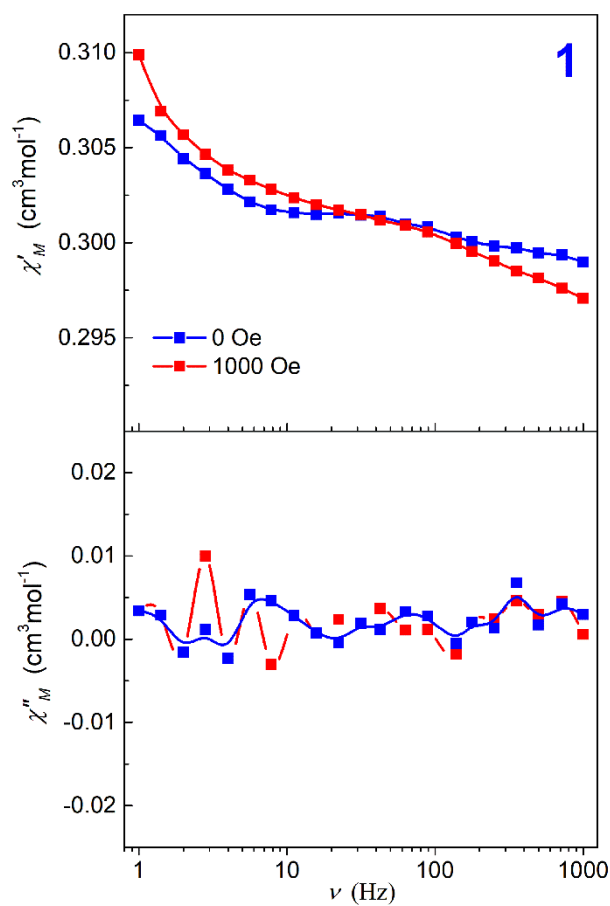


Figure S8. AC susceptibility of 1. The in-phase (χ') and out-of-phase (χ'') components of the ac susceptibility as a function of frequency of complex **1** in 0 and 1000 Oe dc field at 3 K. No peaks were detected suggesting non-SMM behavior of **1**.

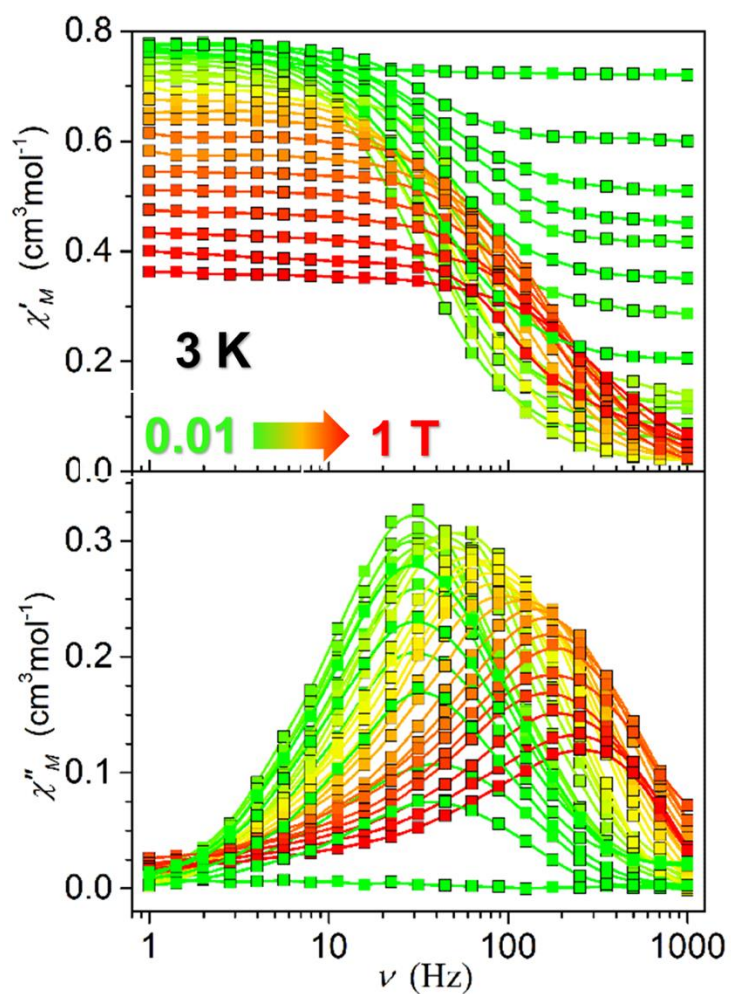


Figure S9. AC susceptibility of 2. Frequency dependence of the in-phase (χ') and out-of-phase (χ'') components of ac magnetic susceptibility of **2** (1–1000 Hz) measured at 3 K in various applied fields from 0.01 to 1 T.

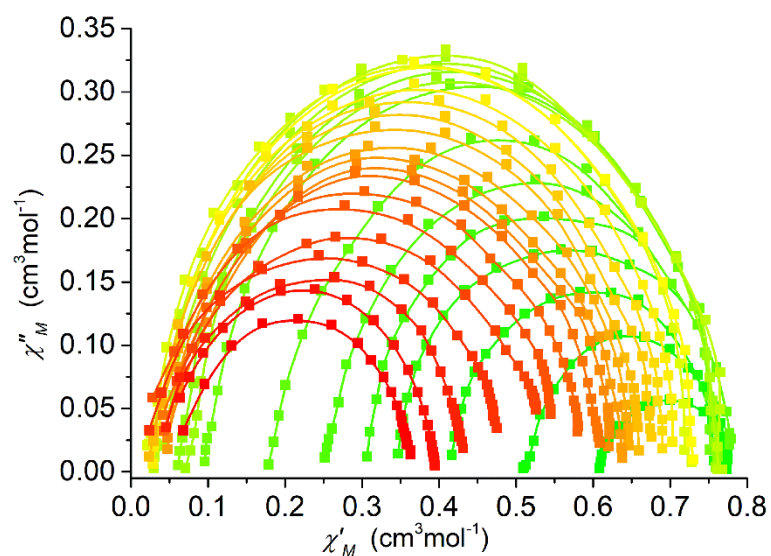


Figure S10. Argand plots of **2.** These Cole–Cole plots were obtained based on the ac magnetic susceptibilities of **2** at 3 K under various applied dc fields. The solid lines represent the best fits of the experimental results with the generalized Debye model.

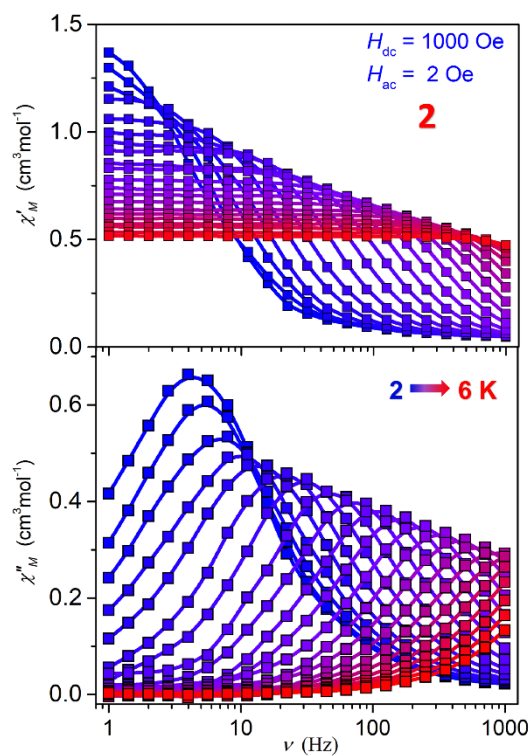


Figure S11. AC susceptibility of 2. The in-phase (χ') and out-of-phase (χ'') components of the ac susceptibility as a function of frequency of **2** in 1000 Oe dc field and at different temperatures as indicated.

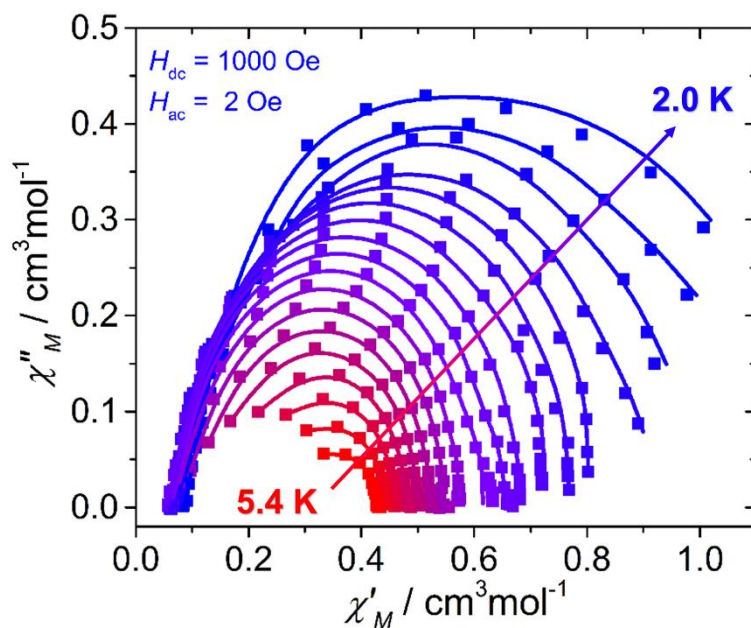


Figure S12. Argand plots of 2. These Cole–Cole plots derived from the frequency-dependent ac susceptibility data of **2** at various temperatures, as indicated. The solid lines represent the best fits of the experimental results with the generalized Debye model.

Table S8. Relaxation fitting parameters at 3 K under different fields from the least-square fitting of the Cole-Cole plots of complex **2** according to the generalized Debye model.

H / Oe	$\chi_S / \text{cm}^3\text{mol}^{-1}\text{K}$	$\chi_T / \text{cm}^3\text{mol}^{-1}\text{K}$	τ / s	α
100	0.60504	0.77656	0.00302	0.24378
200	0.51023	0.77439	0.00345	0.23475
300	0.41142	0.77175	0.00422	0.13404
400	0.33826	0.76684	0.00482	0.13561
500	0.25062	0.75634	0.00566	0.29748
600	0.25595	0.74852	0.00629	0.04884
700	0.17952	0.73732	0.00675	0.07307
800	0.10522	0.74380	0.00712	0.02095
1000	0.06564	0.77285	0.00760	0.04267
1200	0.08374	0.74468	0.00682	0.01845
1400	0.04896	0.75645	0.00614	0.01755
1600	0.03734	0.76112	0.00543	0.02744
1800	0.02746	0.71761	0.00480	0.02156
2000	0.02246	0.70157	0.00417	0.02043
2200	0.03193	0.73074	0.00356	0.05405
2400	0.03219	0.71208	0.00321	0.05783
2600	0.03420	0.70865	0.00274	0.03809
2800	0.02047	0.69288	0.00247	0.08112
3000	0.02475	0.67295	0.00214	0.06388
3200	0.04062	0.65638	0.00181	0.02882
3400	0.02587	0.65103	0.00157	0.08855
3600	0.01493	0.64553	0.00138	0.17552
3800	0.04164	0.62490	0.00123	0.11690
4000	0.03123	0.61426	0.00105	0.00321
4500	0.01377	0.58148	9.5E-4	0.00594
5000	0.01777	0.54318	9.1E-4	0.07552
6000	0.02695	0.51615	9.0E-4	0.09401
7000	0.01472	0.45202	8.8E-4	0.15572
8000	0.04091	0.42800	8.8E-4	0.11552
9000	0.03664	0.39437	8.7E-4	0.15780
10000	0.08002	0.36149	8.7E-4	0.05921

Table S9. Relaxation fitting parameters at different temperatures under 1000 Oe from the least-square fitting of the Cole-Cole plots of complex **2** according to the generalized Debye model.

T / K	$\chi_S / \text{cm}^3\text{mol}^{-1}\text{K}$	$\chi_T / \text{cm}^3\text{mol}^{-1}\text{K}$	τ / s	α
2.0	0.08053	1.1441	0.04687	0.12953
2.2	0.0731	1.05837	0.03469	0.12076
2.4	0.07593	0.96248	0.02237	0.09416
2.6	0.07043	0.88206	0.01412	0.07624
2.8	0.05983	0.81755	0.0088	0.06427
3.0	0.06816	0.76751	0.00559	0.03039
3.2	0.07483	0.71748	0.00369	0.02023
3.4	0.08231	0.68119	0.00248	0.01023
3.6	0.08088	0.6509	0.00171	0.01061
3.8	0.08125	0.62614	0.00121	0.00984
4.0	0.10375	0.57172	8.4E-4	0.00884
4.2	0.11516	0.54178	6.1E-4	0.00641
4.4	0.13587	0.52571	4.8E-4	0.00594
4.6	0.15702	0.49688	3.6E-4	0.00552
4.8	0.19667	0.47946	3E-4	0.00409
5.0	0.22689	0.46395	2.4E-4	0.00459
5.2	0.26646	0.44324	2E-4	0.00152
5.4	0.31128	0.43323	1.6E-4	0.00184

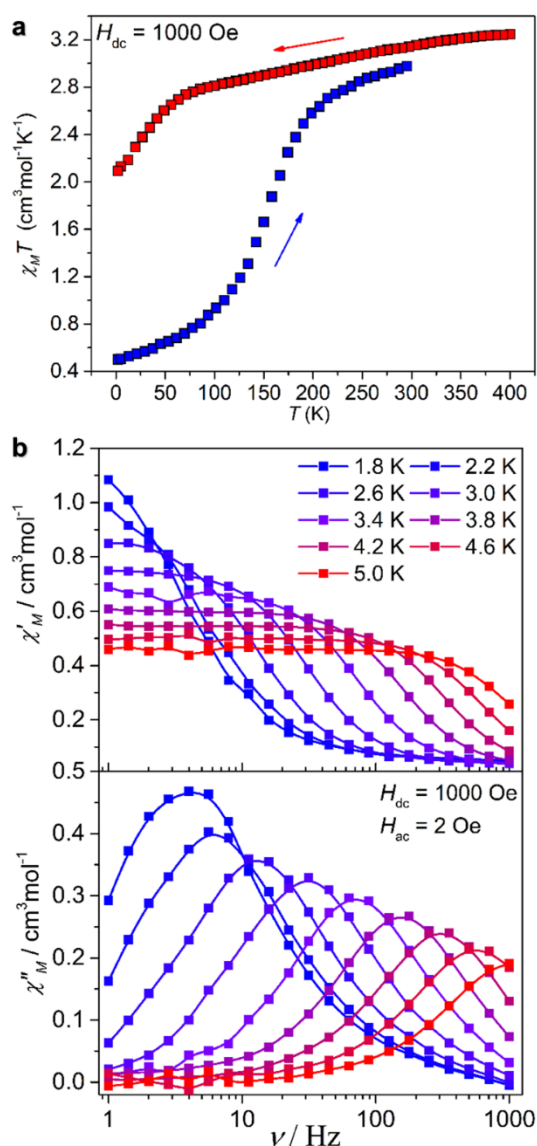


Figure S13. DC and AC susceptibilities of the rehydrated sample and its dehydrated form. **a.** Susceptibility temperature product χT as a function of temperature recorded on a powder sample of **1-re** at an applied field of 1000 Oe following the 2-400-2 K measure sequences; **b.** out-of-phase components of the ac susceptibility as a function of frequency of dehydrated **1-re** in 1000 Oe dc field and at different temperatures of the ac magnetic field as indicated.

Table S10. Significant supramolecular interactions in **1**.

Complex	1	
	300 K	100 K
<i>T</i>		
O2 ···O1	3.36(4)	2.87(5)
O5 ···O2	2.69(8)	2.65(8)
O3 ···O1	2.89(6)	2.79(9)
O4 ···N7	3.00(2)	2.92(5)
O7 ···N8	3.07(8)	2.94(6)
C12H12 ···O5	2.36(8)	2.31(0)
C18H18 ···O6	2.58(1)	2.42(9)
C5H5 ···O1	2.96(4)	2.86(6)
C6H6 ···O1	2.66(0)	2.54(1)
C2H2 ···O3	2.89(1)	2.79(3)
C3H3 ···O5	2.78(5)	2.69(0)
$\pi \cdots \pi^a$	3.65(1)	3.56(9)
a: centroid ···centroid distance between two aromatic rings		

Supplementary discussion of the magnetic relaxation processes in 2. The relaxation mechanisms for a single-ion magnet system are usually very complex and involve multiple relaxation pathways, such as the direct, QTM, Raman, and Orbach relaxation processes.¹⁰ These processes can be described by the following equation including the sum of all four terms:

$$\tau^{-1} = cH^4T + \frac{B_1}{1+B_2H^2} + d \left(\frac{1+eH^2}{1+fH^2} \right) T^n + \tau_0^{-1} \exp(-U_{\text{eff}}/k_B T) \quad (\text{S1})$$

where the first two terms are direct and QTM relaxation processes with coefficients c , B_1 , and B_2 . The third term is the Raman relaxation process, which is both field and temperature dependent. The coefficient d represents the Raman relaxation at zero field, f the ability of the external magnetic field to suppress the internal relaxation mechanisms, and e the attitude of the internal magnetic moments to induce relaxation.¹¹⁻¹³ The first three terms are field dependent, while the last one term represents the contribution of Orbach mechanism, which is field independent.

Usually, thermally activated behaviour observed in high-temperature region is usually attributed to an Orbach relaxation process through the excited $M_S = \pm 1/2$ levels, which can be fitted by Arrhenius equation $\tau = \tau_0 \exp(U_{\text{eff}}/k_B T)$. From the fitting of high temperature data in the Arrhenius plot (Fig. 4b), the U_{eff} is estimated to be 34.1 K (23.6 cm^{-1}). Although the linear part in the high-temperature region in the Arrhenius plot is wide with 12 data points and the Arrhenius fit seems quite good, the obtained U_{eff} is far too small considering the quite large easy-axis magnetic anisotropy. Notably, the Orbach process should involve a “real” transition to an excited magnetic energy level and a relaxation to the ground state. Therefore, the effective energy barrier U_{eff} is expected to be equal or close to the energy gap between the ground doublets and the first excited doublets. For compound **2**, this energy gap is estimated to be around 150 cm^{-1} from the $|2D|$ value or at least 160 cm^{-1} from the calculated energy gap between the ground and the first excited doublets (Table S7). This large energy gap means that there are no intermediate magnetic energy levels for the Orbach process in the present system. Therefore, we think that the Orbach process in **2** is very unlikely and we will

not consider this process in the following analyses of the relaxation times. Anyway, the curve obviously deviates from the linear tendency at low temperatures for **2**, suggesting a multiple relaxation pathway.

To probe the possible relaxation mechanisms involved, the field dependence of the magnetic relaxation times was analyzed firstly. The field dependent relaxation time at 3 K was obtained from the treatment of the ac susceptibility data under different magnetic fields from 0.01 to 1.0 T (insert of Fig. 4b). As we can see, the relaxation time τ increases first from 0.01 T to a maximum value at 0.1 T, and then decrease again to around 0.4 T. Then, τ almost kept unchanged in the field range of 0.4-1.0 T.

This field dependent behavior of τ indicates that at least two relaxation mechanisms are necessary to model the data. From the above eq. S1, we can see that the first three terms are all field dependent. Thus, the field dependence of the magnetic relaxation time was fitted by different models considering two magnetic relaxation mechanisms (direct+Raman, direct+QTM and Raman+QTM). As τ almost kept unchanged above 0.4 T, we only fit the data in the field range of 0.01-0.4 T. The results are plotted in the inset of Fig. 4b. As can be seen, while the rest two combinations (direct+QTM and Raman+QTM) couldn't give a good fitting of the curve, the model involving direct and Raman mechanisms ($\tau^{-1} = cH^4T + d[(1 + eH^2)/(1 + fH^2)]T^n$) could reproduce the field dependence of τ with the best-fit parameters $c = 54.8(9) \text{ T}^{-4}\text{ms}^{-1}$, $d \times T^n = 0.41(7) \text{ ms}^{-1}$, $e = 0.6(2) \times 10^3 \text{ T}^{-2}$, $f = 2.0(8) \times 10^3 \text{ T}^{-2}$ with an Adj.R-Square of 0.97. These results suggest that the direct and Raman relaxation processes should dominate at 3 K, while the QTM term seems not suitable. This is reasonable as the QTM from the transverse zero-field splitting (E) is usually forbidden for the Kramers ions at zero field. In addition, application of a dc field further removes the degeneracy of the $\pm 3/2$ states and suppresses efficiently the QTM effect.

Then, the c , e , and f parameters were fixed using the above obtained values (as for parameters d and n , they couldn't be determined independently from the above fitting), and the Arrhenius plot of **2** under the optimum dc field of 0.1 T was fitted also with the direct and Raman processes ($\tau^{-1} = cH^4T + d[(1 + eH^2)/(1 + fH^2)]T^n = 0.00548 \times T +$

$0.349 \times d \times T^n$), giving $d = 2.0(3) \text{ ms}^{-1}$ and $n = 4.8(2)$ with an Adj.R-Square of 0.99. The very good fitting further proves the dominant direct and Raman relaxation processes in 2. Normally, for the Raman process, n equals 7 and 9 for non-Kramers and Kramers ions, respectively. When optical and acoustic phonons are taken into consideration depending on the structure of energy levels, $n = 1-6$ is also reasonable. Thus, the obtained n value suggests probably optical acoustic Raman process involving a virtual state, where both acoustic and optical phonons are considered.

Supplementary References

- (1) SAINT Software Users Guide, version 7.0; Bruker Analytical X-Ray Systems: Madison, WI, 1999.
- (2) G. M. Sheldrick, SADABS, version 2.03; Bruker Analytical X-Ray Systems, Madison, WI, 2000.
- (3) G. M. Sheldrick, SHELXTL, Version 6.14, Bruker AXS, Inc.; Madison, WI 2000-2003.
- (4) G. Karlström, R. Lindh, P.-A. Malmqvist, B.O. Roos, U. Ryde, V. Veryazov, P.-O. Widmark, M. Cossi, B. Schimmelpfennig, P. Neogrady and L. Seijo, MOLCAS: a Program Package for Computational Chemistry., *Comput. Mater. Sci.*, 2003, 28, 222.
- (5) F. Neese, ORCA—an ab initio, density functional and semiempirical program package, version 4.0.1; Max-Planck institute for bioinorganic chemistry: Mülheim an der Ruhr, Germany, 2017
- (6) A. D. Becke, *J. Chem. Phys.*, 1993, 98, 5648.
- (7) A. D. Becke, *Phys. Rev. A.*, 1988, 38, 3098.
- (8) C. Lee, W. Yang and R. G. Parr, *Phys. Rev. B.*, 1988, 37, 785.
- (9) F. Weigend and R. Ahlrichs, *Phys. Chem. Chem. Phys.*, 2005, 7, 3297.
- (10) J. M. Zadrozny, M. Atanasov, A. M. Bryan, C.-Y. Lin, B. D. Reinken, P. P. Power, F. Neese and J. R. Long, *Chem. Sci.*, 2013, 4, 125–138.
- (11) Van Vleck, J. H. *Phys. Rev.* **1940**, 57, 426.
- (12) M. Atzori, L. Tesi, S. Benci, A. Lunghi, R. Righini, A. Taschin, R. Torre, L. Sorace, and R. Sessoli, *J. Am. Chem. Soc.*, **2017**, 139, 4338-4341.
- (13) M. Atzori, E. Morra, L. Tesi, A. Albino, M. Chiesa, L. Sorace, and R. Sessoli, *J. Am. Chem. Soc.* **2016**, 138, 11234-11244.